

Ferroelectricity induced by lone pair electron effect in halide perovskite monolayers

Junting Zhang^{1,*}, Yu Xie¹, Jun He¹, Ke Ji¹, and Xiaofan Shen^{2,†}

¹*School of Materials Science and Physics, China University of Mining and Technology, Xuzhou 221116, China*

²*National Laboratory of Solid State Microstructures and Physics School, Nanjing University, Nanjing 210093, China*



(Received 25 April 2024; revised 15 June 2024; accepted 8 July 2024; published 16 July 2024)

Two-dimensional (2D) ferroelectricity has attracted considerable interest since its demonstration in van der Waals monolayers. Research on 2D ferroelectricity has so far focused on van der Waals materials, and whether some of the intrinsic ferroelectric mechanisms found in perovskite bulks can be retained to the monolayer limit remains an issue to be solved. Here, we demonstrate that intrinsic ferroelectricity caused by the lone pair electron effect can exist in the inorganic halide perovskite monolayers. This ferroelectricity occurs in halide perovskite monolayers with smaller anions, involving Cs_2GeF_4 , Cs_2SnF_4 , and Cs_2SnCl_4 . The first two are direct band-gap semiconductors while the latter is an indirect band-gap semiconductor. The octahedral tilt mode also appears in the ground-state structures of these 2D ferroelectrics. The ferroelectric monolayers containing F^- ions have relatively greater ferroelectric polarization, but also have a higher-energy barrier for ferroelectric switching. This work helps to design 2D ferroelectricity beyond van der Waals materials.

DOI: [10.1103/PhysRevB.110.035419](https://doi.org/10.1103/PhysRevB.110.035419)

I. INTRODUCTION

Ferroelectrics exhibit an extensive application prospect in many fields such as memory storage, sensors, and optoelectronic devices [1,2]. Reducing the thickness of ferroelectric films has become a key issue in ferroelectric research, which plays an important role in the miniaturization, integration, and low-energy consumption of ferroelectric devices. However, due to the influence of the depolarization field and surface effect, conventional ferroelectrics commonly encounter a critical thickness problem, that is, ferroelectricity disappears when reduced to nanometer size [3–5]. Therefore, whether conventional ferroelectricity can be retained to the two-dimensional (2D) limit has been a long-standing issue [6]. In recent years, breakthroughs have been made in the research on 2D ferroelectricity, which has been confirmed in some van der Waals monolayers such as SnTe , CuInP_2S_6 , and In_2Se_3 [7–10]. At present, research on 2D ferroelectrics is still focused on van der Waals materials, and some novel ferroelectric phenomena have been discovered, such as the emergence of ferroelectricity in elemental monolayers [11], sliding-induced ferroelectricity [12,13], and quantum fractional ferroelectricity [14].

Perovskite ferroelectrics, as the most extensive class of ferroelectrics, have rarely been experimentally achieved in their 2D morphology [5]. A recent theoretical study has predicted the existence of some ferroelectric mechanisms in few-layer perovskite oxides, such as ferroelectricity driven by the d^0 configuration of transition-metal ions, octahedral rotation distortion, or surface effects [15]. Our previous studies have shown that octahedral rotation-induced ferroelectricity

and spin-induced ferroelectricity can be widely present in 2D perovskite systems, which also enable 2D multiferroics with intrinsic magnetoelectric coupling [16–20]. Experimentally, free-standing perovskite oxide monolayers such as SrTiO_3 and BiFeO_3 have been successfully prepared and can be transferred to any desired substrate [21–23], paving the way for the development of perovskite-based 2D ferroelectricity.

Compared with oxide perovskites, halide perovskites have the advantages of a soft structure and easy processing in miniaturizing ferroelectric devices [24–26]. Experimental studies have shown that the inorganic halide perovskite CsPbF_3 transforms from a cubic to rhombohedral phase (space group $R3c$) at temperatures below 187 K, resulting in the emergence of ferroelectricity [27]. From the perspective of environmental protection, Pb-free halide perovskites have more application prospects than Pb-based ones. Recently, ferroelectricity has been experimentally demonstrated in the Ge-based halide perovskites CsGeX_3 ($X = \text{Cl}, \text{Br}, \text{I}$) bulks [28], whose spontaneous ferroelectric polarization can reach $10\text{--}20 \mu\text{C}/\text{cm}^2$. The origin of ferroelectricity is related to the $4s^2$ lone pair electron configuration of Ge^{2+} ions, and these ferroelectrics show an ideal band gap and strong light absorption and photoresponse. Nevertheless, whether such ferroelectricity driven by lone pair electrons can exist in halide perovskite monolayers is a key issue to be studied.

In this paper, we investigated the lattice dynamics, ground-state structure, electronic property, and ferroelectricity of Ge-based and Sn-based halide perovskite monolayers Cs_2MX_4 ($M = \text{Ge}, \text{Sn}; X = \text{F}, \text{Cl}, \text{Br}, \text{I}$) by combining first-principles calculations and symmetry analysis. The results show that intrinsic ferroelectricity driven by the ns^2 lone pair electron configuration exists in halide perovskite monolayers with smaller anions, involving Cs_2GeF_4 , Cs_2SnF_4 , and Cs_2SnCl_4 . Their ground-state structures exhibit simultaneous octahedral tilt and polar displacement distortion. Halogen

*Contact author: juntingzhang@cumt.edu.cn

†Contact author: xiaofan.shen@smail.nju.edu.cn

ions have a significant impact on the ground-state structure, electronic property, and ferroelectricity of these perovskite monolayers.

II. COMPUTATIONAL DETAILS

Our first-principles calculations based on density functional theory (DFT) were performed using the projector augmented-wave (PAW) method [29], as implemented in the Vienna *ab initio* simulation package (VASP) [30]. The Perdew-Burke-Ernzerhof functional modified for solids (PBEsol) [31] within the framework of the generalized gradient approximation (GGA) was used as the exchange-correlation functional. Electronic band structures were also calculated by the Heyd-Scuseria-Ernzerhof (HSE) functional for comparison [32]. The $\sqrt{2} \times \sqrt{2} \times 1$ supercells were used to construct structural phases resulting from various lattice distortion modes in perovskite monolayers. A vacuum space of 15 Å was imposed in order to avoid interlayer interactions between neighboring periodic images. A plane-wave cutoff energy of 600 eV was employed, and a Γ -centered $7 \times 7 \times 1$ k -point mesh was used for the Brillouin zone integration. A convergence threshold of 10^{-6} eV was used for the electronic self-consistency loop. The in-plane lattice constants and internal atomic coordinates of each structure phase were relaxed until the Hellman-Feynman forces were less than 10^{-2} eV/Å on each atom.

Phonon band structures of the prototype and ground-state phases were calculated using density functional perturbation theory (DFPT) [33]. The phonon frequencies and corresponding eigenmodes were calculated by the PHONOPY code [34]. To confirm the thermodynamic stability of the ground-state phase, first-principles molecular dynamics simulations at room temperature were performed in a canonical ensemble using the Nosé heat bath scheme. The climbing nudged elastic band (NEB) method [35] was used to determine the energy barrier of ferroelectric switching. The ISOTROPY tool [36] was used to aid with symmetry analysis.

III. RESULTS AND DISCUSSION

A. Lattice dynamics

The halide perovskite monolayers considered possess a complete octahedral structure, that is, both of its surfaces are A - X layers, as shown in Fig. 1. This monolayer structure can be regarded as a basic building block of layered perovskite bulk A_2BX_4 , and similar terminal surfaces have been observed in the experimentally prepared free-standing 2D perovskite films [22]. In view of the possible structural reconstruction with respect to their bulk phases, we started from the prototype phase of the monolayer (space group $P4/mmm$). The phonon band structures of the prototype phases of all halide perovskite monolayers were calculated to verify their stability and find possible structural distortion modes. Figure 2 shows that the prototype phases of all Sn-based monolayers exhibit unstable vibration modes. The lowest-frequency soft modes appear at the center Γ point or boundary M point of the Brillouin zone, corresponding to the polar displacement and the antipolar octahedral distortion (rotation or deformation), respectively. As the anion radius increases, the lowest-frequency soft modes transition from polar distortion

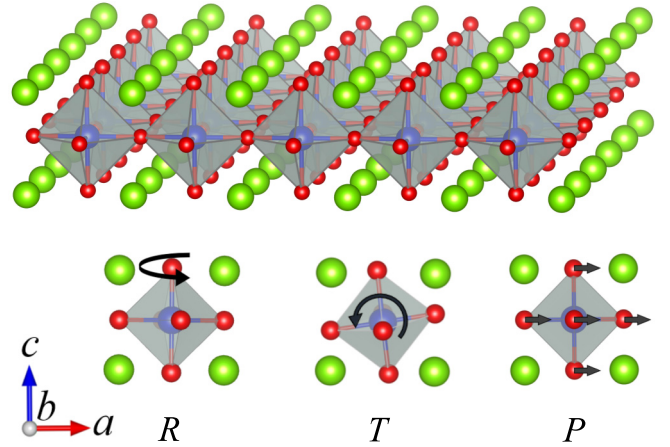


FIG. 1. Crystal structure of the perovskite monolayer and schematic diagrams of the three lattice distortion modes involving octahedral rotation (R), tilt (T), and polar displacement (P). Curved arrows represent the rotation direction of the octahedron, and straight arrows represent the direction of anion displacement.

to octahedral distortion, which may be attributed to the decrease of the perovskite tolerance factor. As for the Ge-based monolayers, all the prototype phases are dynamically stable except Cs_2GeF_4 . The polar soft modes in this monolayer show an obvious instability, similar to the Cs_2SnF_4 monolayer.

We then investigated which distortion modes appear to reduce the energy of the system. For the in-plane polar displacement mode belonging to the irreducible representation Γ_5^- , only the Cs_2SnF_4 and Cs_2GeF_4 monolayers exhibit typical double-well energy curves, and the latter shows relatively greater energy gain, as shown in Figs. 3(a) and 3(b). In contrast, the in-plane polar mode of other monolayers and the out-of-plane polar mode (Γ_3^-) of all monolayers show parabolic energy curves.

Octahedral rotation distortion, the most common type of lattice distortion in perovskites, can be divided into rotation and tilt modes in 2D perovskites, corresponding to the rotation of octahedron around the out-of-plane and in-plane axes, respectively (see Fig. 1). The rotation and tilt (out-of-phase) modes belong to the irreducible representations M_2^+ and M_5^+ , respectively. The latter has three types of order parameters $M_5^+(a, 0)$, $M_5^+(a, a)$, and $M_5^+(a, b)$, which represents the octahedral rotation axis along the $[110]$, $[100]$, and the general direction of the prototype phase, respectively. Figures 4 and 5 show the energy curves of octahedral rotation and tilt modes for Sn-based and Ge-based halide perovskite monolayers, respectively. Of all monolayers, only the Cs_2SnF_4 monolayer shows energy gain for the octahedral rotation and tilt distortion modes, which can greatly and slightly reduce the energy of the system, respectively.

B. Ground-state structure

Next, in order to determine the ground-state structure of these halide perovskite monolayers, different structural phases resulting from each lattice distortion mode and their various combinations were considered. For comparison, the antiferroelectric modes and the out-of-plane polar mode were also

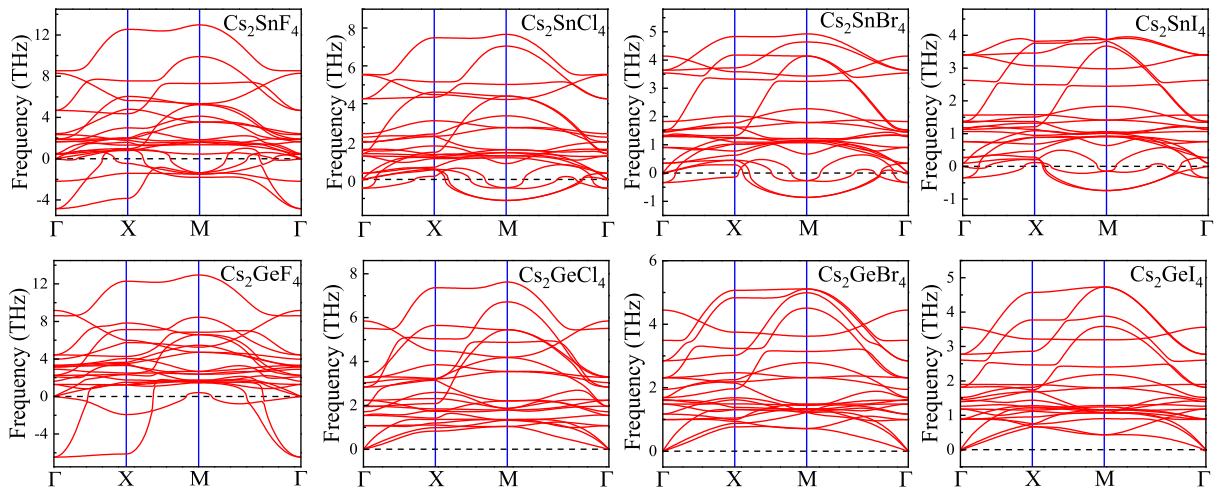


FIG. 2. Phonon band structures of the prototype phases for all halide perovskite monolayers.

included. We calculated the energy of each structural phase by optimizing the lattice constants and atomic coordinates. As shown in Table I, some structural phases cannot exist stably, since some or all lattice distortion modes disappear after structural optimization, resulting in a change in their symmetry. The out-of-plane polar mode (Γ_3^-) can only be stable in the Cs_2SnF_4 monolayer, whose structural phase has very high energy with respect to the in-plane polar mode (Γ_5^-), indicating that the out-of-plane polar mode is suppressed by the depolarization field. Similarly, the out-of-plane antiferroelectric mode (M_2^-) can only be stable in monolayers containing F ions, whose energy is very close to that of the prototype energy. The in-plane polar and antiferroelectric (M_5^-) modes can be stable in more monolayers (mainly Sn-based monolayers), where the former has a relatively lower energy. Note that the combination of the antiferroelectric mode with the rotation or

tilt mode will either establish an existing polar phase or be unstable, therefore, only the combinations of the polar mode with other modes are shown.

For Ge-based monolayers, all structural phases containing lattice distortion are unstable except for the Cs_2GeF_4 monolayer. That is, all distorted structural phases change to the prototype phase after structural optimization, consistent with the results of phonon band structures. For the Cs_2GeF_4 monolayer, the structural phases caused by the in-plane polar mode and its combination with rotation or tilt mode can exist stably, in which the structural phase (space group $Pnc2$) established by polar plus tilt modes has the lowest energy. This polar ground-state phase exhibits an in-plane polarization along the tilt axis.

For the Sn-based monolayer system, many structural phases can be stable, but as the anion radius increases, some structural phases become unstable (see Table I). Only for the Cs_2SnF_4 monolayer, the energy of the structural phase caused by the in-plane polar mode is significantly lower than that

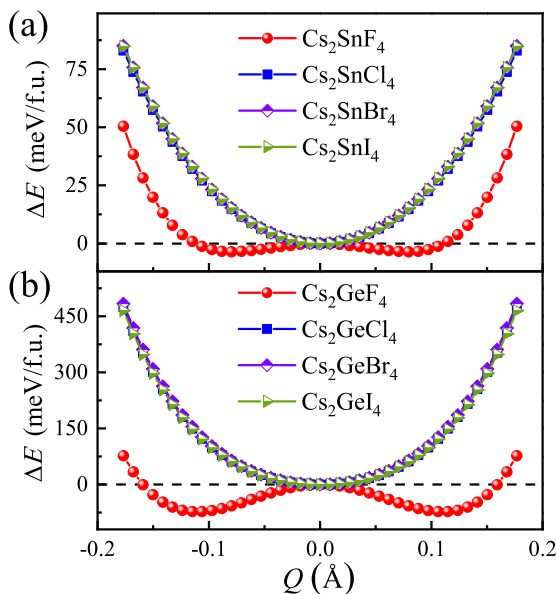
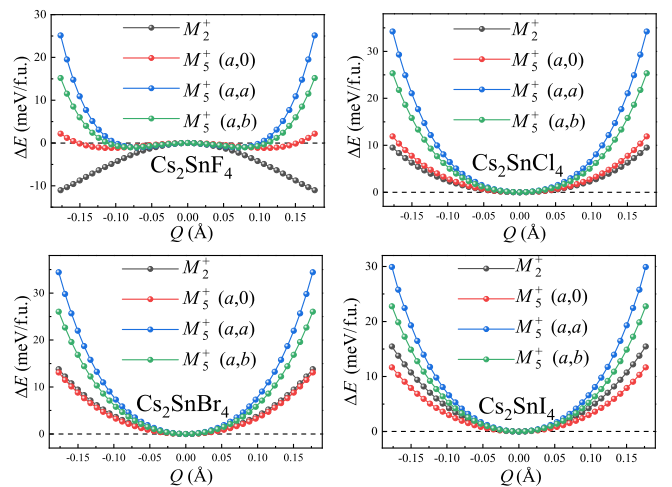


FIG. 3. Variation of energy with the amplitude of the in-plane polar distortion for (a) Sn-based and (b) Ge-based halide perovskite monolayers.


 FIG. 4. Variation of energy with the amplitude of the rotation (M_2^+) and tilt (M_5^+) modes for Sn-based halide perovskite monolayers.

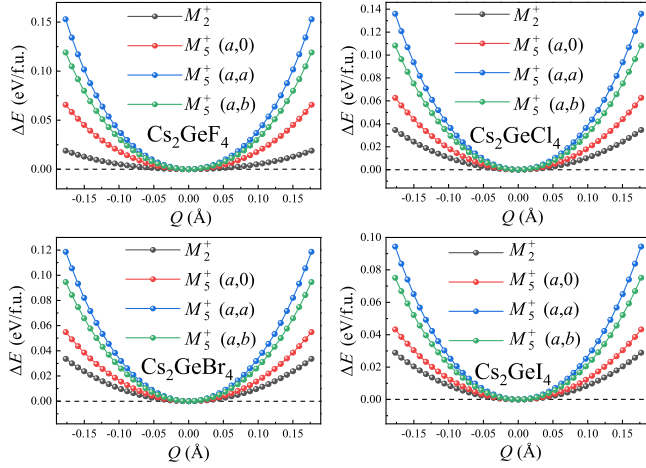


FIG. 5. Variation of energy with the amplitude of the rotation (M_2^+) and tilt (M_5^+) modes for Ge-based halide perovskite monolayers.

of the prototype phase, consistent with the results regarding energy gain. For Cs_2SnF_4 and Cs_2SnCl_4 monolayers, the ground-state structures result from a combination of polar and

TABLE I. Symmetry and energy of structural phases resulting from each distortion mode and their various combinations. The symbol “-” indicates that the corresponding structural phase is unstable, since its symmetry has changed due to the disappearance of some distortion modes after structural optimization.

Distortion modes	Space group	ΔE (meV/f.u.)							
		Cs_2SnX_4				Cs_2GeX_4			
		F	Cl	Br	I	F	Cl	Br	I
Γ_1^+	$P4/mmm$	321	76	52	57	289	0	0	0
Γ_3^-	$P4mm$	257	-	-	-	-	-	-	-
$\Gamma_5^-(a,0)$	$Pmm2$	81	75	52	56	114	-	-	-
$\Gamma_5^-(a,a)$	$Amm2$	65	76	52	57	48	-	-	-
M_2^+	$P4/mbm$	276	-	-	-	-	-	-	-
M_2^-	$P4/nmm$	321	-	-	-	285	-	-	-
$M_5^+(a,0)$	$Pmna$	296	27	0	0	-	-	-	-
$M_5^+(a,a)$	$Cmma$	298	38	9	5	-	-	-	-
$M_5^-(a,0)$	$Cmmm$	313	75	52	-	-	-	-	-
$M_5^-(a,a)$	$Pmma$	312	74	52	58	-	-	-	-
$M_2^+ \oplus \Gamma_5^-(a,0)$	$Amm2$	65	76	52	57	48	-	-	-
$M_2^+ \oplus \Gamma_5^-(a,a)$	$Pmc2_1$	18	75	51	56	47	-	-	-
$M_2^+ \oplus M_5^+(a,0)$	$P2_1/c$	276	-	-	-	-	-	-	-
$M_2^+ \oplus M_5^+(a,a)$	$C2/m$	276	-	-	-	-	-	-	-
$M_2^+ \oplus M_2^-$	$P42_12$	276	-	-	-	-	-	-	-
$M_5^+(a,0) \oplus \Gamma_3^-$	$Pma2$	250	-	-	-	-	-	-	-
$M_5^+(a,a) \oplus \Gamma_3^-$	$Cmm2$	251	-	-	-	-	-	-	-
$M_5^+(a,b) \oplus \Gamma_5^-(c,d)$	Pc	0	-	-	-	-	-	-	-
$M_5^+(a,0) \oplus \Gamma_5^-(b,b)$	$Pnc2$	25	0	-	-	0	-	-	-
$M_5^+(a,0) \oplus \Gamma_5^-(b,-b)$	$Pmm2_1$	127	-	-	-	-	-	-	-
$M_2^+ \oplus M_5^+(a,b) \oplus \Gamma_5^-(c,d)$	$P1$	5	-	-	-	-	-	-	-
$M_2^+ \oplus M_5^+(a,a) \oplus \Gamma_5^-(a,0)$	Cm	39	-	-	-	-	-	-	-

tilt modes. The difference between these two polar ground-state structures is reflected in the different directions of polar displacement, resulting in Pc and $Pnc2$ space groups, respectively. In contrast, for Cs_2SnBr_4 and Cs_2SnI_4 monolayers with larger anions, the ground-state structure is a nonpolar $Pmna$ phase caused by the single tilt mode. These are consistent with the results of the phonon band structures of the prototype phase, that is, the most unstable soft mode transitions from polar to octahedral rotation distortion as the anion radius increases. Therefore, the polar ground-state phase tends to occur in halide perovskite monolayers with smaller anions, which have relatively larger perovskite tolerance factors.

In order to verify the stability of three halide perovskite monolayers with polar ground-state phases, we calculated their phonon band structures and performed first-principles molecular dynamics simulations, which confirm the dynamical and thermodynamical stability of their ground-state phases, respectively, as shown in Fig. 6. The x component of the polar displacement oscillates with a nonzero average, indicating that the polar order can be retained at room temperature.

C. Electronic property

Then the electronic property of the three ferroelectric monolayers was investigated. Considering that DFT calculation may underestimate the band gap, both the PBE functional and the more accurate hybrid functional HSE06 were used to calculate the projected band structure for comparison. As shown in Figs. 7(a)–7(c), the projected band structures of the three ferroelectric monolayers exhibit similar characteristics. The highest occupied valence bands and the lowest unoccupied conduction bands are formed by the outermost s and p orbitals of the B -site cations, respectively. The highest occupied valence bands show significant orbital hybridization characteristics, that is, the s orbitals are mixed simultaneously with the p orbitals of the B -site cations and anions. This may be attributed to the relatively high steric activation energy of the ns^2 electron configuration of the B -site cations, which causes the s - p orbital hybridization and forms covalent bonds with the anions to reduce the energy. This s - p orbital hybridization effect is further demonstrated by the spatial charge distributions for the highest occupied valence bands. As shown in Fig. 8, the s - p hybridization results in an asymmetric distribution of valence electrons for B -site cations, which extends to the closer anions to strengthen the covalent bonds. This obvious s - p orbital hybridization is a manifestation of ferroelectricity induced by the lone pair electron mechanism [37].

The valence band maximum of the three monolayers all appears at the Γ point. The difference is that the conduction band minimum of Cs_2GeF_4 and Cs_2SnF_4 monolayers appears at the Γ point, while it appears in the path from the Γ to the Y point for the Cs_2SnCl_4 monolayer, as shown in Figs. 7(a)–7(c). Therefore, the former two are direct band-gap semiconductors, while the latter is an indirect band-gap semiconductor. The projected band structures calculated by the HSE functional are basically consistent with those of PBE, except for the difference in band gap. The values of band gap calculated by the HSE functional are 4.18, 4.21, and 3.05 eV for Cs_2GeF_4 , Cs_2SnF_4 , and Cs_2SnCl_4 monolayers, respec-

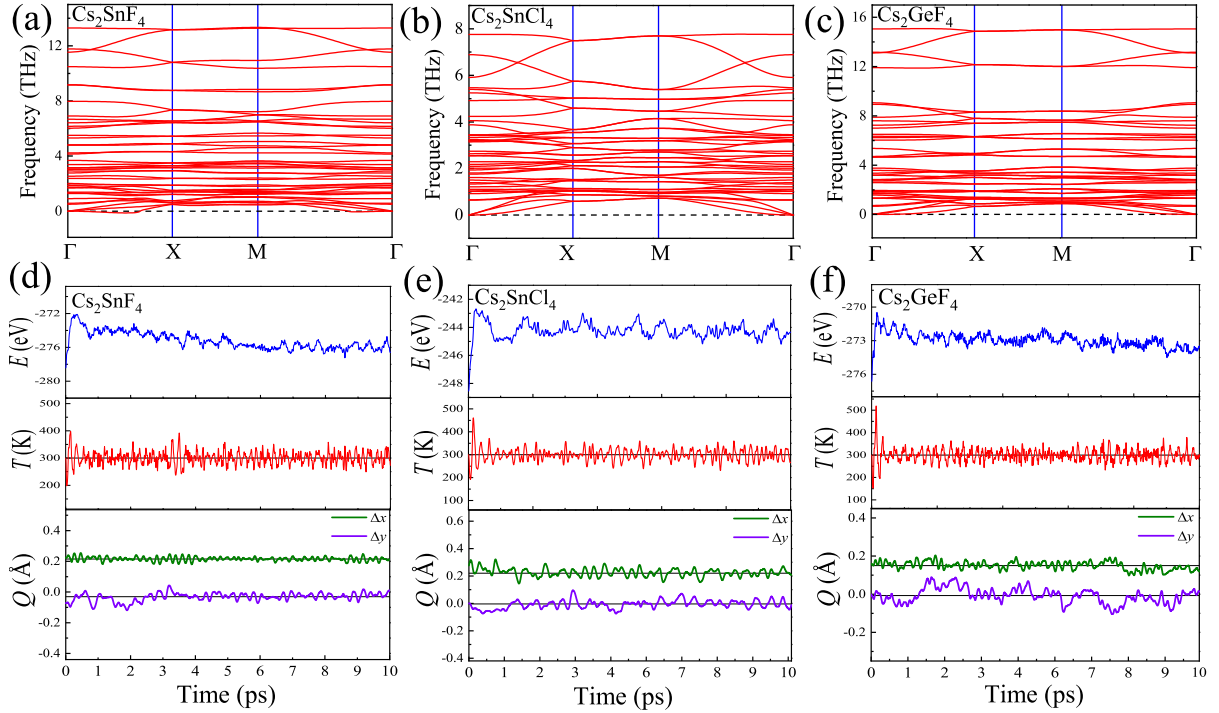


FIG. 6. Phonon band structures of the ground-state phases for (a) Cs_2SnF_4 , (b) Cs_2SnCl_4 , and (c) Cs_2GeF_4 monolayers, as well as (d)–(f) the corresponding first-principles molecular dynamics simulations at 300 K. Energy, temperature, and the average polar displacement of the A-site ions are shown as functions of time.

tively, which are all larger than those of the PBE functional. In addition, for all halide perovskite monolayers, the band gap gradually decreases with increasing anion radius, which may be related to the enhancement of covalency due to the weakening of the electronegativity of the anions.

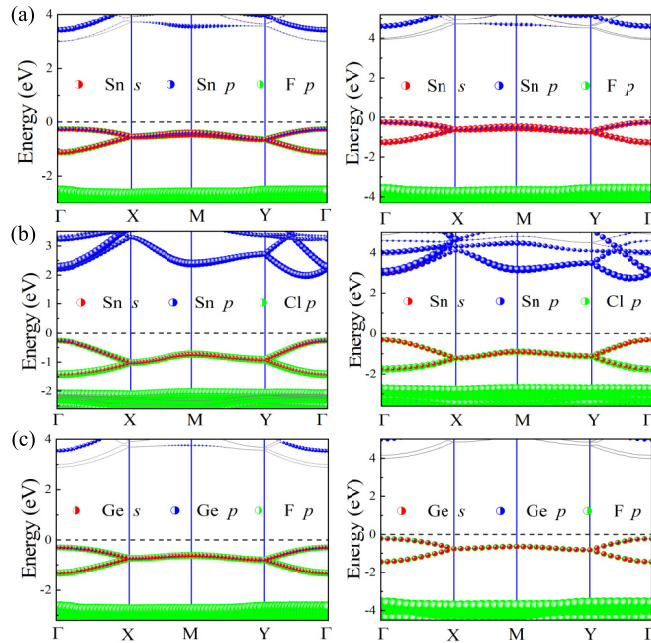


FIG. 7. Projected band structures of the ground-state phases of the (a) Cs_2SnF_4 , (b) Cs_2SnCl_4 , and (c) Cs_2GeF_4 monolayers. The left and right subpanels show the projected band structures calculated by PBE and HSE06 functions, respectively.

D. Ferroelectricity

Next, we investigated the Born effective charge (BEC) and ferroelectric polarization of the three ferroelectric monolayers. As shown in Table II, the B-site cations exhibit anomalously large BEC, significantly exceeding their formal valence +2. In addition, the BEC further increases with increasing anion radius, which is similar to the results of halide perovskite bulks [28]. This anomalously large BEC is related to the ns^2 lone pair electron configuration, and is also a significant characteristic of intrinsic ferroelectricity [37]. Unlike the halide perovskite bulks, ferroelectricity emerges in the perovskite bulks CsGeX_3 ($X = \text{Cl}, \text{Br}, \text{I}$), but disappears in their monolayers [28]. The loss of interlayer coupling leads to the reconstruction of octahedral rotation type, which may be responsible for the difference in ferroelectricity between the bulks and their monolayers [38,39].

In perovskite monolayers, both octahedral rotation and tilt modes retain spatial inversion symmetry and thus do not

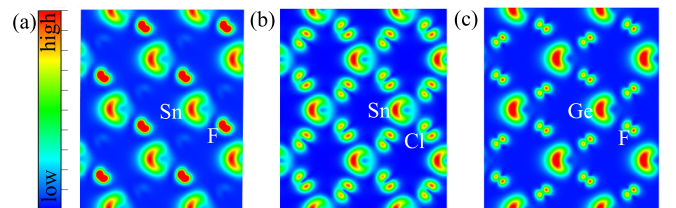


FIG. 8. Spatial charge distributions of the highest occupied valence bands for (a) Cs_2SnF_4 , (b) Cs_2SnCl_4 , and (c) Cs_2GeF_4 monolayers.

TABLE II. Space group, perovskite tolerance factor (t), BEC, ferroelectric polarization (P), and energy barrier of ferroelectric switching for the three ferroelectric monolayers.

Cs_2MX_4	Space group	t	BEC	P ($\mu\text{C}/\text{cm}^2$)	Barrier (meV/f.u.)
Cs_2SnF_4	Pc	1.00	3.5	21.8	293
Cs_2SnCl_4	$Pnc2$	0.95	4.4	9.9	30
Cs_2GeF_4	$Pnc2$	1.10	3.6	37.3	284

contribute to ferroelectric polarization, so the ferroelectric polarization only originates from the polar displacement mode. Among the three 2D ferroelectrics, the Cs_2GeF_4 monolayer with a relatively large tolerance factor ($t = 1.10$) exhibits the largest ferroelectric polarization, reaching $37.3 \mu\text{C}/\text{cm}^2$. Its high ferroelectric polarization is related to the anomalously large displacement of the anions in the middle layer. The Cs_2SnCl_4 monolayer with a relatively small tolerance factor ($t = 0.95$) exhibits the smallest ferroelectric polarization of $9.9 \mu\text{C}/\text{cm}^2$, while the Cs_2SnF_4 monolayer with a tolerance factor of $t = 1$ has the polarization value of $21.8 \mu\text{C}/\text{cm}^2$.

During the ferroelectric switching, the polarization of the three ferroelectric monolayers changes from $+P$ in the initial polarization state to 0 in the intermediate phase and then to $-P$ in the final polarization state (see Fig. 9). The difference is that only the polarization component P_x emerges in the Cs_2GeF_4 and Cs_2SnCl_4 monolayers, while the Cs_2SnF_4 monolayer has two in-plane polarization components P_x and P_y , which are simultaneously reversed during the ferroelectric switching. However, the P_y component is very weak, resulting in ferroelectric polarization dominated by the P_x component.

For Cs_2SnF_4 and Cs_2SnCl_4 monolayers, the intermediate states of ferroelectric switching are structural phases containing only tilt mode, with energy barriers of 293 and 30 meV/f.u., respectively. In contrast, for the Cs_2GeF_4 monolayer, the prototype phase becomes the intermediate state, because the structural phase containing only the tilt mode cannot exist stably (see Fig. 9). Therefore, its ferroelectric switching is accompanied by a change in octahedral tilt distortion, resulting in a relatively high-energy barrier of 284 meV/f.u. Note that the energy barriers are slightly different from the energy of the corresponding structural phases shown in Table I, due to the different optimization methods used, that is, the unit cell volume is fixed and relaxed respectively during the structure optimization process. These results indicate that halogen ions can significantly affect the ferroelectricity of halide perovskite monolayers. Ferroelectric monolayers containing F^- ions have greater ferroelectric polarization and a higher-energy barrier. This can be attributed to the smaller anion radius and stronger bonding for the monolayers containing F^- ions, which results in a larger anion displacement in the middle plane.

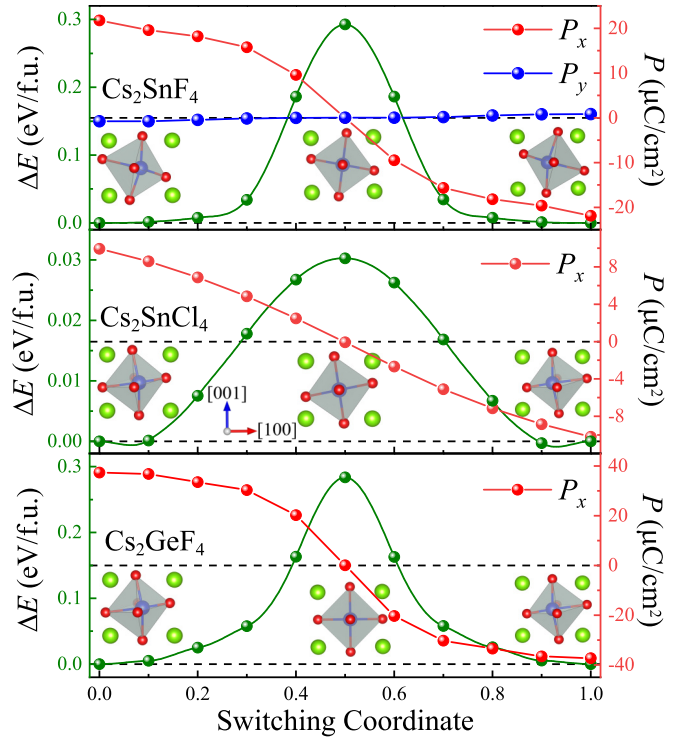


FIG. 9. Variation of relative energy (ΔE) and polarization components (P) of the three ferroelectric monolayers along the ferroelectric switching path. The insets show the structures of the initial state, barrier, and final state of ferroelectric switching.

IV. CONCLUSION

In conclusion, we systematically studied the lattice dynamics, ground-state structure, electronic property, and ferroelectricity of Sn-based and Ge-based halide perovskite monolayers. Ferroelectricity induced by the lone pair electron mechanism can exist in the monolayer limit. This intrinsic ferroelectricity occurs in perovskite monolayers containing F^- or Cl^- ions, and octahedral tilt distortion is also present in their ground-state structures. Halogen ions have significant effects on the structural, electronic property, and ferroelectricity. The monolayers containing F^- ions exhibit larger band gaps, higher ferroelectric polarization, and energy barriers of ferroelectric switching. This work contributes to the discovery and exploration of 2D ferroelectrics based on halide perovskites.

ACKNOWLEDGMENTS

This work was supported by the National Natural Science Foundation of China (Grants No. 12374097 and No. 11974418) and Postgraduate Research Practice Innovation Program of Jiangsu Province (Grant No. KYCX23_0097). Computer resources provided by the High Performance Computing Center of Nanjing University are gratefully acknowledged.

[1] M. Dawber, K. M. Rabe, and J. F. Scott, Physics of thin-film ferroelectric oxides, *Rev. Mod. Phys.* **77**, 1083 (2005).

[2] J. F. Scott, Applications of modern ferroelectrics, *Science* **315**, 954 (2007).

- [3] V. Petkov, V. Buscaglia, M. T. Buscaglia, Z. Zhao, and Y. Ren, Structural coherence and ferroelectricity decay in submicron- and nano-sized perovskites, *Phys. Rev. B* **78**, 054107 (2008).
- [4] J. Junquera and P. Ghosez, Critical thickness for ferroelectricity in perovskite ultrathin films, *Nature (London)* **422**, 506 (2003).
- [5] D. D. Fong, G. B. Stephenson, S. K. Streiffer, J. A. Eastman, O. Auciello, P. H. Fuoss, and C. Thompson, Ferroelectricity in ultrathin perovskite films, *Science* **304**, 1650 (2004).
- [6] P. Gao, Z. Zhang, M. Li, R. Ishikawa, B. Feng, H.-J. Liu, Y.-L. Huang, N. Shibata, X. Ma, S. Chen, J. Zhang, K. Liu, E.-G. Wang, D. Yu, L. Liao, Y.-H. Chu, and Y. Ikuhara, Possible absence of critical thickness and size effect in ultrathin perovskite ferroelectric films, *Nat. Commun.* **8**, 15549 (2017).
- [7] K. Chang, J. W. Liu, H. C. Lin, N. Wang, K. Zhao, A. Zhang, F. Jin, Y. Zhong, X. P. Hu, W. H. Duan, Q. M. Zhang, L. Fu, Q.-K. Xue, X. Chen, and S.-H. Ji, Discovery of robust in-plane ferroelectricity in atomic-thick SnTe, *Science* **353**, 274 (2016).
- [8] F. Liu, L. You, K. L. Seyler, X. Li, P. Yu, J. Lin, X. Wang, J. Zhou, H. Wang, H. He, S. T. Pantelides, W. Zhou, P. Sharma, X. Xu, P. M. Ajayan, J. Wang, and Z. Liu, Room-temperature ferroelectricity in CuInP₂S₆ ultrathin flakes, *Nat. Commun.* **7**, 12357 (2016).
- [9] W. Ding, J. Zhu, Z. Wang, Y. Gao, D. Xiao, Y. Gu, Z. Zhang, and W. Zhu, Prediction of intrinsic two-dimensional ferroelectrics in In₂Se₃ and other III₂-VI₃ van der Waals materials, *Nat. Commun.* **8**, 14956 (2017).
- [10] C. X. Zheng, L. Yu, L. Zhu, J. L. Collins, D. Kim, Y. D. Lou, C. Xu, M. Li, Z. Wei, Y. Zhang, M. T. Edmonds, S. Q. Li, J. Seidel, Y. Zhu, J. Z. Liu, W.-X. Tang, and M. S. Fuhrer, Room temperature in-plane ferroelectricity in van der Waals In₂Se₃, *Sci. Adv.* **4**, eaar7720 (2018).
- [11] C. C. Xiao, F. Wang, S. Y. A. Yang, Y. H. Lu, Y. P. Feng, and S. B. Zhang, Elemental ferroelectricity and antiferroelectricity in group-V monolayer, *Adv. Funct. Mater.* **28**, 1707383 (2018).
- [12] M. H. Wu and P. Jena, The rise of two-dimensional van der Waals ferroelectrics, *WIREs Comput. Mol. Sci.* **8**, e1365 (2018).
- [13] L. Li and M. H. Wu, Binary compound bilayer and multilayer with vertical polarizations: two-dimensional ferroelectrics, multiferroics, and nanogenerators, *ACS Nano* **11**, 6382 (2017).
- [14] J. Y. Ji, G. L. Yu, C. S. Xu, and H. J. Xiang, Fractional quantum ferroelectricity, *Nat. Commun.* **15**, 135 (2024).
- [15] J. Lu, W. Luo, J. Feng, and H. Xiang, Unusual ferroelectricity in two-dimensional perovskite oxide thin films, *Nano Lett.* **18**, 595 (2018).
- [16] Y. Zhou, S. Dong, C. X. Shan, K. Ji, and J. T. Zhang, Two-dimensional ferroelectricity induced by octahedral rotation distortion in perovskite oxides, *Phys. Rev. B* **105**, 075408 (2022).
- [17] J. T. Zhang, X. F. Shen, Y. C. Wang, C. Ji, Y. Zhou, J. L. Wang, F. Z. Huang, and X. M. Lu, Design of two-dimensional multiferroics with direct polarization-magnetization coupling, *Phys. Rev. Lett.* **125**, 017601 (2020).
- [18] X. F. Shen, Q. Y. Luo, Z. S. Wu, Y. Zhou, J. L. Wang, J. T. Zhang, J. Su, and X. M. Lu, Magnetoelectric coupling dependent on ferroelectric switching paths in two-dimensional perovskite multiferroics, *Phys. Rev. B* **103**, L220406 (2021).
- [19] J. T. Zhang, Y. Zhou, F. Wang, X. F. Shen, J. L. Wang, and X. M. Lu, Coexistence and coupling of spin-induced ferroelectricity and ferromagnetism in perovskites, *Phys. Rev. Lett.* **129**, 117603 (2022).
- [20] X. F. Shen, F. Wang, X. M. Lu, and J. T. Zhang, Two-dimensional multiferroics with intrinsic magnetoelectric coupling in A-site ordered perovskite monolayers, *Nano Lett.* **23**, 735 (2023).
- [21] S. S. Hong, J. H. Yu, D. Lu, A. F. Marshall, Y. Hikita, Y. Cui, and H. Y. Hwang, Two-dimensional limit of crystalline order in perovskite membrane films, *Sci. Adv.* **3**, eaao5173 (2017).
- [22] H. Wang, Z. R. Liu, H. Y. Yoong, T. R. Paudel, J. X. Xiao, R. Guo, W. N. Lin, P. Yang, J. Wang, G. M. Chow, T. Venkatesan, E. Y. Tsymbal, H. Tian, and J. S. Chen, Direct observation of room-temperature out-of-plane ferroelectricity and tunneling electroresistance at the two-dimensional limit, *Nat. Commun.* **9**, 3319 (2018).
- [23] D. Ji, S. Cai, T. R. Paudel, H. Sun, C. Zhang, L. Han, Y. Wei, Y. Zang, M. Gu, Y. Zhang, W. Gao, H. Huyan, W. Guo, D. Wu, Z. Gu, E. Y. Tsymbal, P. Wang, Y. Nie, and X. Pan, Freestanding crystalline oxide perovskites down to the monolayer limit, *Nature (London)* **570**, 87 (2019).
- [24] W. L. Zheng, X. C. Wang, X. Zhang, B. Chen, H. Suo, Z. F. Xing, Y. Z. Wang, H. Wei, J. K. Chen, Y. Guo, and F. Wang, Emerging halide perovskite ferroelectrics, *Adv. Mater.* **35**, 2205410 (2023).
- [25] J. Y. Qian, B. Xu, and W. J. Tian, A comprehensive theoretical study of halide perovskites ABX₃, *Org. Electron.* **37**, 61 (2016).
- [26] W.-Q. Liao, Y. Zhang, C.-L. Hu, J.-G. Mao, H.-Y. Ye, P.-F. Li, S. D. Huang, and R.-G. Xiong, A lead-halide perovskite molecular ferroelectric semiconductor, *Nat. Commun.* **6**, 7338 (2015).
- [27] P. Berastegui, S. Hull, and S.-G. Eriksson, A low-temperature structural phase transition in CsPbF₃, *J. Phys.: Condens. Matter* **13**, 5077 (2001).
- [28] Y. Zhang, E. Parsonnet, A. Fernandez, S. M. Griffin, H. Huyan, C.-K. Lin, T. Lei, J. Jin, E. S. Barnard, A. Raja, P. Behera, X. Pan, R. Ramesh, and P. Yang, Ferroelectricity in a semiconducting all-inorganic halide perovskite, *Sci. Adv.* **8**, eabj5881 (2022).
- [29] P. E. Blöchl, Projector augmented-wave method, *Phys. Rev. B* **50**, 17953 (1994).
- [30] G. Kresse and J. Furthmüller, Efficient iterative schemes for *ab initio* total-energy calculations using a plane-wave basis set, *Phys. Rev. B* **54**, 11169 (1996).
- [31] J. P. Perdew, A. Ruzsinszky, G. I. Csonka, O. A. Vydrov, G. E. Scuseria, L. A. Constantin, X. Zhou, and K. Burke, Restoring the density-gradient expansion for exchange in solids and surfaces, *Phys. Rev. Lett.* **100**, 136406 (2008).
- [32] J. Heyd, G. E. Scuseria, and M. Ernzerhof, Hybrid functionals based on a screened Coulomb potential, *J. Chem. Phys.* **118**, 8207 (2003).
- [33] X. Gonze and C. Lee, Dynamical matrices, born effective charges, dielectric permittivity tensors, and interatomic force constants from density-functional perturbation theory, *Phys. Rev. B* **55**, 10355 (1997).
- [34] A. Togo and I. Tanaka, First principles phonon calculations in materials science, *Scr. Mater.* **108**, 1 (2015).
- [35] D. Sheppard, P. H. Xiao, W. Chemelewski, D. D. Johnson, and G. Henkelman, A generalized solid-state nudged elastic band method, *J. Chem. Phys.* **136**, 074103 (2012).

- [36] B. J. Campbell, H. T. Stokes, D. E. Tanner, and D. M. Hatch, ISODISPLACE: A web-based tool for exploring structural distortions, *J. Appl. Crystallogr.* **39**, 607 (2006).
- [37] Y. P. Fu, S. Jin, and X. Y. Zhu, Stereochemical expression of ns^2 electron pairs in metal halide perovskites, *Nat. Rev. Chem.* **5**, 838 (2021).
- [38] E. H. Smith, N. A. Benedek, and C. J. Fennie, Interplay of octahedral rotations and lone pair ferroelectricity in CsPbF₃, *Inorg. Chem.* **54**, 8536 (2015).
- [39] Y. P. Fu, Stabilization of metastable halide perovskite lattices in the 2D limit, *Adv. Mater.* **34**, 2108556 (2022).